

Biogenic sulfur gases as biosignatures on temperate sub-Neptune waterworlds

SHANG-MIN TSAI ¹, HAMISH INNES ^{2,3}, NICHOLAS F. WOGAN ^{4,5} AND EDWARD W. SCHWIETERMAN ^{1,5,6}

¹*Department of Earth and Planetary Sciences, University of California, Riverside, CA, USA*

²*Atmospheric, Oceanic and Planetary Physics, Department of Physics, University of Oxford, UK*

³*Freie Universität Berlin, Institute of Geological Sciences, Malteserstrasse 74-100, 12249 Berlin, Germany*

⁴*Space Science Division, NASA Ames Research Center, Moffett Field, CA 94035*

⁵*Virtual Planetary Laboratory, University of Washington, Seattle, WA 98195*

⁶*Blue Marble Space Institute of Science, Seattle, WA, USA*

ABSTRACT

Theoretical predictions and observational data indicate a class of sub-Neptune exoplanets may have water-rich interiors covered by hydrogen-dominated atmospheres. Provided suitable climate conditions, such planets could host surface liquid oceans. Motivated by recent JWST observations of K2-18 b, we self-consistently model the photochemistry and potential detectability of biogenic sulfur gases in the atmospheres of temperate sub-Neptune waterworlds for the first time. On Earth today, organic sulfur compounds produced by marine biota are rapidly destroyed by photochemical processes before they can accumulate to significant levels. Domagal-Goldman et al. (2011) suggest that detectable biogenic sulfur signatures could emerge in Archean-like atmospheres with higher biological production or low UV flux. In this study, we explore biogenic sulfur across a wide range of biological fluxes and stellar UV environments. Critically, the main photochemical sinks are absent on the nightside of tidally locked planets. To address this, we further perform experiments with a 3D GCM and a 2D photochemical model (VULCAN 2D (Tsai et al. 2024)) to simulate the global distribution of biogenic gases to investigate their terminator concentrations as seen via transmission spectroscopy. Our models indicate that biogenic sulfur gases can rise to potentially detectable levels on hydrogen-rich waterworlds, but only for enhanced global biosulfur flux ($\gtrsim 20$ times modern Earth’s flux). We find that it is challenging to identify DMS at $3.4 \mu\text{m}$ where it strongly overlaps with CH_4 , whereas it is more plausible to detect DMS and companion byproducts, ethylene (C_2H_4) and ethane (C_2H_6), in the mid-infrared between 9 and $13 \mu\text{m}$.

1. INTRODUCTION

The Kepler mission revealed a large fraction of discovered planets with radii between Earth and Neptune (Howard et al. 2012; Thompson et al. 2018; Bean et al. 2021). Observed masses and radii indicate a population of sub-Neptunes likely containing water-rich interiors, while evolution models also point to the existence of these waterworlds on the population scale (Zeng et al. 2019; Venturini et al. 2020; Luque & Pallé 2022; Rogers et al. 2023). In particular, several such planets orbiting M dwarf stars receive comparable instellation¹ to Earth, placing them in their planetary systems’ habitable zones (e.g., Table 1 in Madhusudhan et al. (2021)). These temperate sub-Neptunes have sparked great interest in atmospheric characterization and the assessment of habitability. Given suitable climate conditions (Pierrehumbert 2023; Innes et al. 2023), these water-rich worlds could host surface water oceans below hydrogen-rich atmospheres – recently referred to as “Hycean” (Hydrogen ocean) worlds (Madhusudhan et al. 2021; Nixon & Madhusudhan 2021). Promisingly, their hydrogen-rich envelopes are more favorable for atmospheric characterization in transmission observations due to large scale heights, compared to the higher molecular weight N_2 - or CO_2 -dominated atmospheres.

Since the water detection in the atmosphere of the temperate sub-Neptune K2-18 b (Benneke et al. 2019; Tsias et al. 2019), follow-up analyses and modeling efforts have sought to unveil the nature of K2-18 b and similar temperate sub-Neptunes. Madhusudhan et al. (2020) explored the bulk composition under different interior structures. Yu

¹ insolation from their host stars

et al. (2021); Tsai et al. (2021b) proposed using atmospheric compositional evolution to infer the presence of a shallow surface, whereas Hu et al. (2021) investigated the carbon inventories in a Hycean planet scenario. Recent JWST transit observations revealed a strong detection of carbon dioxide (CO_2) and methane (CH_4) on K2-18 b (Madhusudhan et al. 2023). Based on this basis and upper limits of carbon monoxide (CO) and ammonia (NH_3), Madhusudhan et al. (2023) argued that the atmospheric characteristics of K2-18 b are more consistent with a Hycean world scenario. However, several inconsistencies warrant consideration: (1) It is challenging to accumulate % level of CH_4 without biological input or thermochemical recycling from the interior (Yu et al. 2021; Tsai et al. 2021b). (2) On Hycean planets, CO can still be efficiently produced to around 0.1 – 1 % level through photolysis of CO_2 , while the quenched CO abundance is controlled by the interior temperature on Neptune-like planet with a thick ($\gtrsim 100$ bar) H_2 -atmosphere (Wogan et al. 2024). (3) The cross-correlation method may be required to identify CO in JWST NIRSpec data (Esparza-Borges et al. 2023), while current analysis based on a single transit observation might not be sufficient to conclusively rule out NH_3 before the upcoming MIRI and revisit observations (JWST Cycle 1, GO-2722 and GO-2372).

Intriguingly, Madhusudhan et al. (2023) also reported a tentative detection of dimethylsulfide (DMS), which is predominately produced by marine microbes on Earth and regarded as a biosignature gas, especially for anoxic biospheres (see Domagal-Goldman et al. (2011) and Schwieterman et al. (2018) for a review). On modern Earth, DMS is the main biological source of sulfur, about $1.8\text{--}3.5 \times 10^9$ molecules $\text{cm}^{-2}\text{s}^{-1}$ (Seinfeld & Pandis 2016; Cala et al. 2023). DMS and methanethiol (CH_3SH) are released from the degradation of dimethylsulfoniopropionate (DMSP), an organosulfur compound produced by marine phytoplankton. Microbial methylation and detoxification processes can also actively produce DMS from hydrogen sulfide (H_2S) (Li et al. 2023), allowing hypothetical organisms to make use of the H_2S reservoir in a H_2 -rich environment on Hycean worlds. In addition, decayed organic substances in the surface ocean can produce carbon disulfide (CS_2) and carbonyl sulfide (OCS) through photochemical processes. These biosulfur gases are not directly associated with energy generation but are products or byproducts of physiological responses, referred to as Type III Biosignatures in Seager et al. (2013). On present-day Earth, these organic sulfur gases are readily destroyed through photolysis or oxidation by OH radicals (Kettle et al. 2001; Domagal-Goldman et al. 2011) and thus cannot accumulate to significant concentrations exceeding the ppm level required for remote detection.

While great uncertainties persist regarding how biology could operate in an H_2 -rich atmosphere, useful analogies can be drawn from anoxic environments on Earth. As early microbial life emerged, the Archean atmosphere was more reducing than present-day, with abundant CO_2 and CH_4 (e.g., Catling & Zahnle 2020). As indicated by genomic analysis, organic sulfur cycling could date back to the Proterozoic (Mateos et al. 2023), while sulfur-based metabolic pathways likely emerged in Earth’s earliest biosphere in the Archean and may have been common for biological evolution (Pilcher 2003; House et al. 2003). On Archean Earth-like worlds, most biogenic sulfur gases are rapidly destroyed in the atmosphere similar to the present-day, except with the major sink being the reaction with atomic O produced by photolysis (Domagal-Goldman et al. 2011). Curiously, the potential sulfur-based biosignatures and chemical pathways within a H_2 -dominated atmosphere have not yet been fully explored with self-consistent photochemistry. Moreover, many close-in sub-Neptunes around M stars might be tidally locked. On the permanent nightside, such photochemical sinks of these organic sulfur gases do not exist. It is therefore essential to quantify whether the biogenic gases can build up on the terminators where transit observations probe.

In this Letter, we explore the global distribution and detectability of methane- and sulfur-based biosignature gases on Hycean planets through photochemical and climate modeling. While there is currently no robust evidence that K2-18 b is a Hycean planet, we adopt its properties as a paradigmatic example for Hycean exoplanets overall.

2. METHODS

Here, we model the atmospheric composition of a Hycean planet under a range of biological surface emissions. Using the planetary parameters of K2-18 b as a fiducial example, we vary the surface flux of biosulfur gases and stellar UV flux to quantify the impacts on the global composition of Hycean planet atmospheres.

2.1. 1D climate and photochemical models

We iterate the radiative transfer (HELIOS; Malik et al. (2019a); Malik et al. (2019b)) and photochemical (VULCAN; Tsai et al. (2017, 2021)) models to obtain a self-consistent 1D temperature profile of Hycean K2-18 b. The radiative transfer model HELIOS has been modified to include the moist adiabatic lapse rate in the convective adjustment

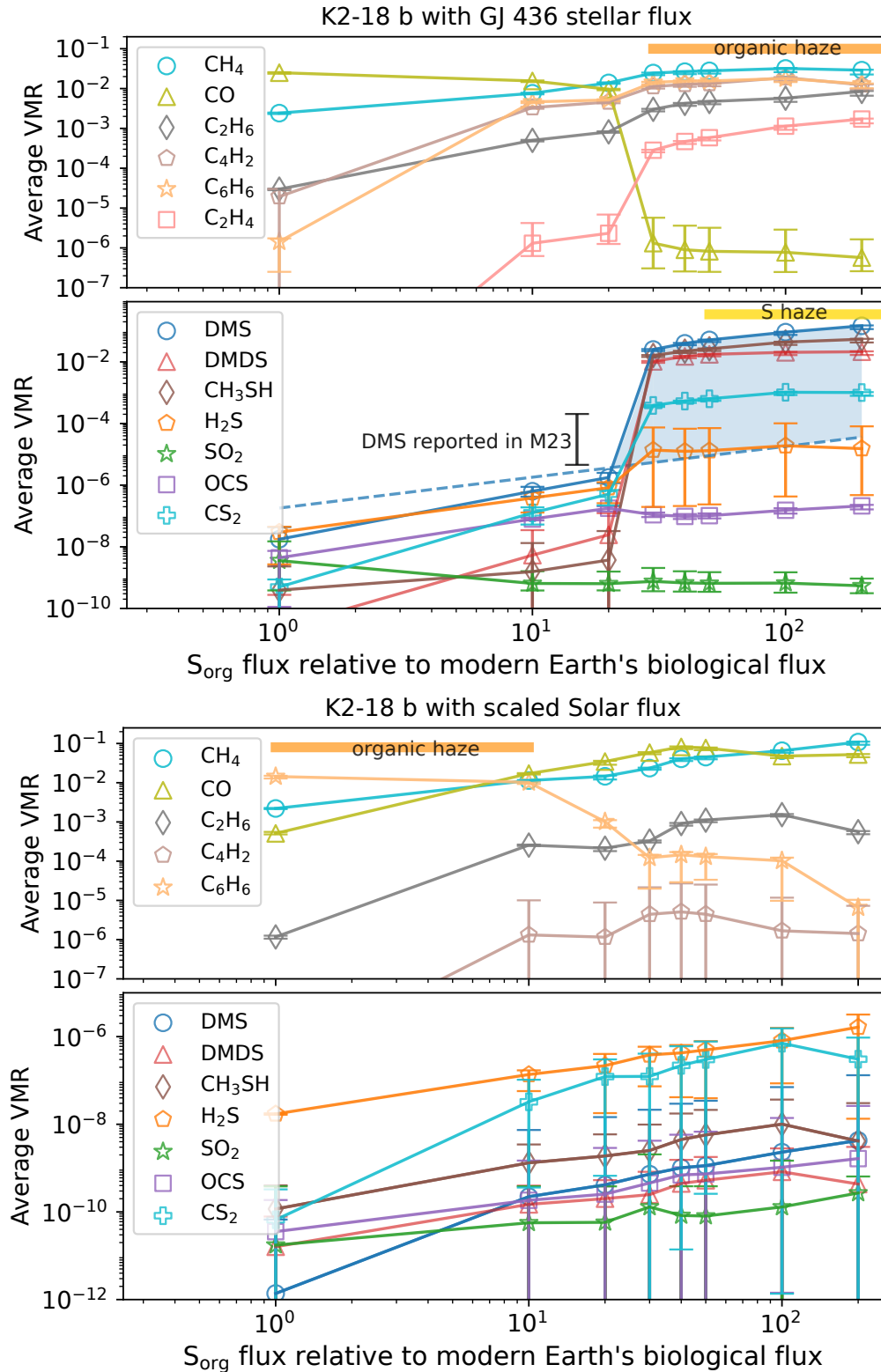


Figure 1. The average volume mixing ratios (VMRs) as a function of sulfur biological flux (S_{org}). We adopt the stellar spectrum of GJ 436 as an analogous star to K2-18 for our nominal Hycean K2-18 b model (top). Additionally, we scaled the solar flux to match an equivalent flux (bottom). Open circles are the average VMRs across the 1 to 10^{-4} bar pressure range, whereas error bars denote the full span of VMRs within this pressure range. The dashed line represents the limit of DMS given by surface deposition with 0.01 cm^{-1} dry deposition velocity. Combined with the deposition-free DMS abundances in our model, the shaded blue region illustrates the upper and lower bounds of DMS abundance. The black error bar marks the reported DMS VMR from [Madhusudhan et al. \(2023\)](#) (M23). The orange band highlights the regime where hydrocarbon haze precursors, C_4H_2 and C_6H_6 , exceed 1%. Similarly, the yellow band highlights the regime where elemental sulfur (S_8) becomes saturated and condenses.

steps to simulate atmospheres with condensing components². For our nominal Hycean planet, we assume a 1-bar H₂-dominated atmosphere with elements given by 100 × solar metallicity, following (Yu et al. 2021; Tsai et al. 2021b). We fix the surface composition of CO₂, N₂, and H₂O in the lower boundary conditions. CO₂ is set to 1% at the surface, based on the retrieved CO₂ abundance in Madhusudhan et al. (2023) and in accordance with the carbon-inventory estimates in Kite & Ford (2018) and Hu et al. (2021). Surface N₂ is fixed to 0.006, corresponding to all nitrogen (from the 100 × solar metallicity) partitioning into N₂. The water vapor is assumed to be saturated above the ocean with a relative humidity of 50%. The spectrum of an analogous M2.5 star GJ 436 is adopted for both HELIOS and VULCAN.

To achieve a marginally habitable surface temperature, we employ an ad hoc surface albedo of 0.3, as previous studies have indicated that highly reflective clouds are necessary to prevent a runaway greenhouse state on K2-18 b (Piette & Madhusudhan 2020; Innes et al. 2023). Similarly, we do not account for the possibility of convection inhibition, which would otherwise raise the surface temperature beyond the supercritical point of water (Innes et al. 2023; Pierrehumbert 2023). This allowed us to model a habitable atmospheric state supportive of liquid surface water. The temperature and composition profiles are iterated between HELIOS and VULCAN until the temperature change is about 1%. The planetary parameters for our K2-18 b Hycean model are listed in Table A1.

The self-consistent temperature and composition structures of our “lifeless” K2-18 b Hycean planet (excluding biological surface fluxes) are illustrated in Figure A1. We then fed the temperature profile into VULCAN to model the compositional evolution in response to various biological surface fluxes. We updated the S–N–C–H–O photochemical network by revising the reactions involving H₂CO (see Appendix B and Wogan et al. (2024)) and introduced reactions related to dimethyl sulfide (DMS) and dimethyl disulfide (DMDS)³. We consider CH₄ released from methanogenesis and a range of organic sulfur gases biologically emitted from the surface, including CH₃SH, CS₂, DMS, dimethyl disulfide (DMDS), and OCS, collectively termed “S_{org}” after Domagal-Goldman et al. (2011). During this stage, the temperature profile from lifeless Hycean is held fixed and we neglect the thermal feedback from the compositional variations due to biological input (mainly CH₄ and S_{org}).

The rates of gases deposited to the ocean depend on the aerodynamics at the atmosphere-ocean interface and the solubility of the gas (Hu et al. 2012; Seinfeld & Pandis 2016). Due to the uncertainty of parameterizing the dry deposition velocities of several organic sulfur compounds, we assume zero dry deposition for CH₃SH, DMS, DMDS, and CS₂, corresponding to the upper limit of biosignature accumulation where biogenic sulfur compounds saturate the oceanic mixed layer. The lower boundary conditions with modern Earth global average S_{org} flux are described in Appendix A and Table A3.

² <https://github.com/exoclimate/HELIOS/tree/development>

³ https://github.com/exoclimate/VULCAN/blob/master/thermo/SNCHO_DMS_photo_network.Tsai2024.txt

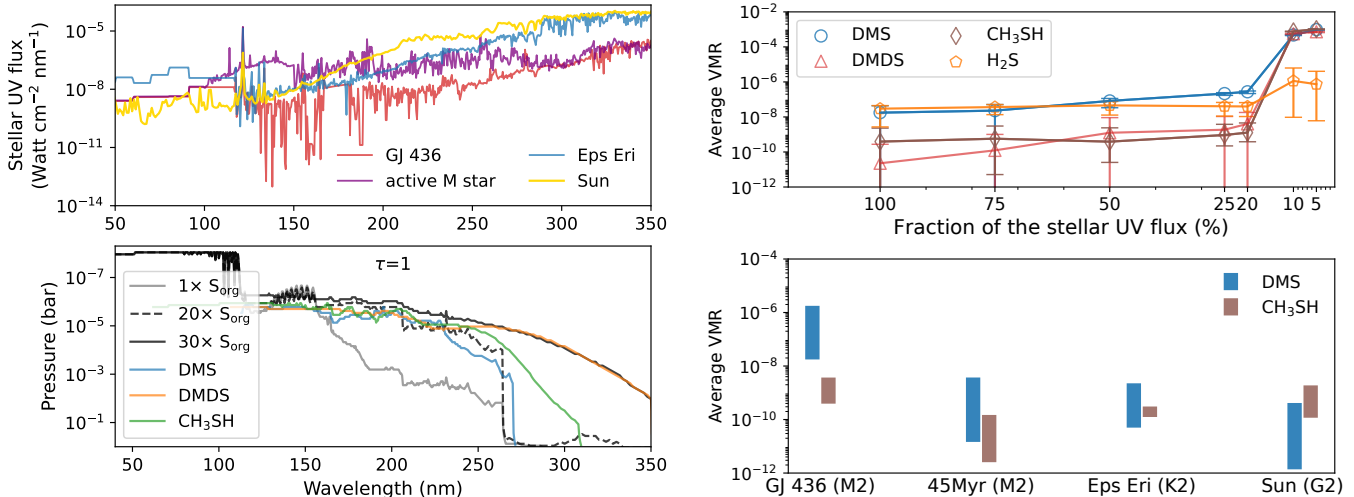


Figure 2. Left: The stellar spectra in the UV for GJ 436 (M2.5), a young (45 Myr) and active M star, Epsilon Eridani, and the Sun in the top panel. The spectra of GJ 436 and Epsilon Eridani are from the MUSCLES survey (version 2.2) (France et al. 2016; Youngblood et al. 2016; Loyd et al. 2016), the active M star spectrum is from HAZMAT (Peacock et al. 2020), and the solar spectrum is from Gueymard (2018). The lower panel shows the UV photosphere ($\tau = 1$) with different S_{org} . The contributions from DMS, DMDS, and CH_3SH are further displayed for the $30\times S_{\text{org}}$ model. Right: The upper panel shows the average VMRs of several sulfur species as a function of attenuating total stellar UV flux for Earth’s S_{org} flux. The bottom panel shows the span of abundance averaged between 1 and 10^{-4} bar for $1\times - 20\times S_{\text{org}}$ flux around different stellar types

2.2. 3D GCM 2D photochemical model

In the absence of photochemical destruction, biological sulfur compounds can in principle build up on the night side of a tidally-locked Hycean planet. Global circulation plays a central role in transporting species between the dayside and nightside, where distinct chemical sources and sinks are at play (Chen et al. 2018; Tsai et al. 2021b; Tsai et al. 2023c). To account for the day-night transport, we run VULCAN 2D (Tsai et al. 2021b; Tsai et al. 2024) to model the equatorial region, using temperature and wind structures from the 3D GCM ExoFMS (Lee et al. 2021; Innes & Pierrehumbert 2022) as input.

ExoFMS has previously been used to model the climate of a warmer K2-18 b (surface temperature > 500 K) without a liquid ocean and water condensation (Innes & Pierrehumbert 2022). In this study, we fit the shortwave and longwave band opacities in ExoFMS to match our 1D HELIOS correlated-k results. Therefore, the double-gray opacities in our Exo-FMS roughly represent the opacities from the self-consistent $100\times$ solar metallicity composition. The input parameters are listed in Table A1 and the temperature and wind structures can be found in Figure A2.

The temperatures and winds obtained from exo-FMS are averaged over the equatorial region across 30° and divided into 32 longitude columns to set up VULCAN 2D. In VULCAN 2D, the zonal winds from the GCM are directly implemented for east-west advection, while vertical transport is parameterized by the eddy diffusion coefficient (K_{zz}) derived from the mixing length theory with $K_{zz} = 0.1 H \times w_{\text{rms}}$, assuming $0.1\times H$ (scale height) as the characteristic length (Smith 1998; Charnay et al. 2015). We use the same lower boundary conditions as the 1D model uniformly across all longitudes.

3. RESULTS

3.1. 1D: S_{org} flux $\gtrsim 20\times$ modern Earth value is required to accumulate ppm-levels of DMS

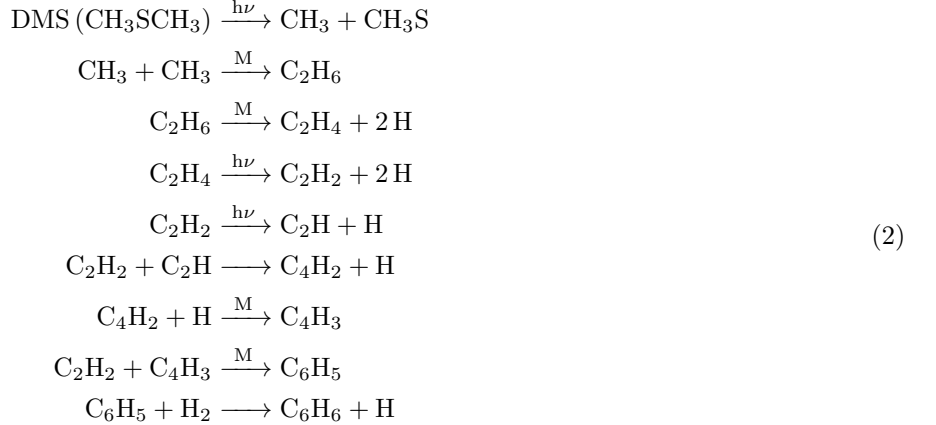
Figure 1 illustrates the average mixing ratios of several carbon-bearing and organic sulfur species in response to increases of biological production of sulfur gases. With modern Earth’s S_{org} flux, surface DMS reaches abundances of around 1–30 ppb, before being destroyed above 0.01 bar in our Hycean K2-18 b model. The DMS concentrations on Hycean K2-18 b are slightly higher than modern and Archean Earth’s values, which are around 0.01–1 ppb levels (Zhang et al. 2020; Domagal-Goldman et al. 2011). As the S_{org} flux continues increasing, there is an abrupt transition between 20–30 times S_{org} flux in our S_{org} -deposition-free setup. After this threshold, the atmosphere becomes rich in organic sulfur species and poor in CO, while CH_3SH , DMS, and DMDS jump from sub-ppm level to above 0.1 %.

In the more conservative scenario where the ocean is not saturated, DMS is expected to be limited by the surface deposition and increased linearly with increasing S_{org} , as shown by the dashed line in Figure 1. Once S_{org} exceeds $20\text{--}30\times$ Earth’s value, H_2S begins accumulating in the upper atmosphere, as a result of photochemistry reducing sulfur back to its thermochemically favored state. This occurs when CH_3SH builds up to sufficiently high abundances that its photodissociation becomes significant, producing H_2S via the following pathway



In fact, the ultimate fate of S_{org} species in a Hycean atmosphere is either photochemical oxidation into CH_3SO or reduction back to hydrocarbons and H_2S , where CH_3SO is mainly produced by DMDS reacting with atomic O. The path to H_2S becomes more dominant over CH_3SO as S_{org} flux increases and makes the atmosphere more reducing. Although SO_2 is also photochemically produced, it is highly soluble and deposition into the ocean limits abundances to insignificant levels.

Notably, the atmosphere also becomes rich in hydrocarbons as S_{org} increases, as pointed out in Domagal-Goldman et al. (2011). CO follows an opposite trend to S_{org} , showing an abrupt decline after 20 times modern Earth’s S_{org} flux. In this carbon-rich regime, the high abundances of haze precursors, such as C_4H_2 and C_6H_6 (Tsai et al. 2021), imply that the atmosphere would be covered by photochemical hazes (Arney et al. 2018). A main pathway to produce organic haze precursors in the upper atmosphere initiated by DMS photolysis is



For DMS at low concentrations below ppm-level, its primary sink is direct photodissociation. After the transition to where DMS has a high concentration, its photodissociation halts in the lower atmosphere due to shielding by DMDS, CH_3SH , and self-shielding. The reaction with atomic H becomes the main sink. This shielding effect from S_{org} also reduces the photolysis of CO_2 causing the drop of CO when the flux $\gtrsim 20\times S_{\text{org}}$. The overall impact of shielding across this transition is evident in the top left panel of Figure 2, where DMS, DMDS, and CH_3SH significantly elevate the near-UV (NUV) photosphere and subsequently attenuate the NUV flux reaching the surface.

For an equivalent solar flux, the same average abundances of hydrocarbon and sulfur gases as a function of biological sulfur flux are shown in the bottom of Figure 1. One major difference is that the stronger NUV irradiation generates atomic H down to the surface, which significantly suppresses DMS and other organic sulfur gases. DMS remains below 10 ppb level for S_{org} flux up to 200 times modern Earth’s value. Moreover, the concentration of DMS is confined near the surface, whereas for an M-dwarf host star, DMS can extend vertically above 0.01 bar. Since S_{org} never reaches significant abundances under a Sun-like star, shielding of CO_2 photolysis does not occur. Consequently, both CH_4 and CO progressively increase with S_{org} flux. Our model results with an active M star show qualitatively similar trends to those with the equivalent solar flux owing to its enhanced UV flux.

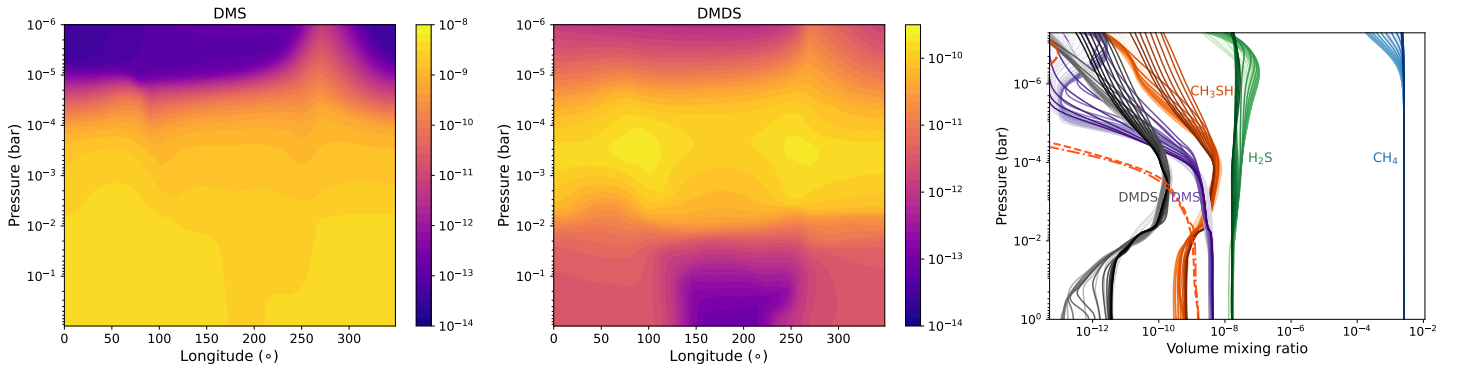
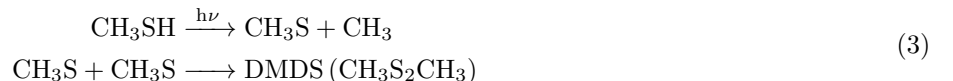


Figure 3. The equatorial volume-mixing-ratio distribution of DMS (left) and DMDS (middle) in our Hycean K2-18 b model with modern Earth S_{org} flux, computed by VULCAN 2D. The substellar point is located at 180° longitude. The right panel depicts the vertical distribution of several species across the equatorial region, where different shades correspond to different longitudinal locations. The vertical profiles of DMS excluding zonal transport are shown in red dotted (morning terminator, 73° westward sub-stellar point) and dashed-dotted (evening terminator, 73° eastward sub-stellar point) lines for comparison.

3.2. 2D: DMS is homogenized by global circulation

The temperature and wind structures simulated by our Hycean K2-18 b GCM can be found in Figure A2. The circulation exhibits an eastward zonal jet in the troposphere and day-night thermally driven cells in the stratosphere. In the upper atmosphere above 10^{-4} bar, the flow transitions to retrograde, likely due to vertical momentum transport (Tsai et al. 2014). The mean tropospheric zonal wind below 0.01 bar is about 20 m/s, consistent with the jet speed estimated from wave balance (Hammond et al. 2020). This zonal wind speed translates to a horizontal transport timescale of ~ 10 days.

Figure 3 illustrates the equatorial distribution of DMS and DMDS for modern Earth S_{org} production. DMS exhibits a rather uniform abundance below 10^{-4} bar. As the zonal winds change to retrograde in the upper atmosphere, DMS extends to higher altitudes around the evening terminator due to the westward transport from the nightside. On the other hand, DMDS is photochemically produced by CH_3SH via



in the stratosphere between 10^{-2} – 10^{-4} bar and follows the thermally driven cells. This relatively uniform distribution of DMS can be understood by comparing relevant timescales. The photochemical lifetime of DMS on the dayside ($\tau_{\text{DMS}}^{\text{day}}$) is determined by $\tau_{\text{DMS}}^{\text{day}} = 1/k_{\text{DMS}}$, where k_{DMS} is its photolysis rate. $\tau_{\text{DMS}}^{\text{day}}$ is $\sim 10^8$ – 10^9 s in the troposphere below 10^{-2} bar. On the nightside, the replenish timescale ($\tau_{\text{DMS}}^{\text{night}}$) is given by $\sim H/K_{zz}^2 \sim 10^8$ s. Given that $\tau_{\text{DMS}}^{\text{day}}$ and $\tau_{\text{DMS}}^{\text{night}}$ are comparable to each other and considerably longer than the horizontal transport timescale of $\sim 10^6$ s, the S_{org} species on the nightside is still constrained by the photochemical processes on the dayside through global transport. We note that our 2D model already assumes an optimistic scenario with a uniform S_{org} flux across the nightside. In reality, the nightside S_{org} flux might be much lower due to the lack of stellar energy input to power a (hypothetical) photosynthetic biosphere. Overall, the DMS abundance predicted by our 2D photochemical model is broadly consistent with that from 1D model, as indicated by the right panel in Figure 3.

3.3. Transmission spectra

We simulated synthetic transmission spectra of our cloud-/haze-free Hycean K2-18 b models using PLATON (Zhang et al. 2019, 2020), including opacity sources of CH_4 , CO , CO_2 , C_2H_2 , H_2O , HCN , NH_3 , O_2 , NO , C_2H_4 , C_2H_6 , H_2CO , N_2 , NO_2 , H_2S , COS , SH , SO_2 , (CIA) of H_2 – H_2 and H_2 – He . We further include cross-sections of CH_3SH , DMS, and DMS from the Pacific Northwest National Laboratories (PNNL) database (Johnson et al. 2004), which are limited to 1 bar pressure and room temperature.

The transmission spectra for none, $1\times$ and $20\times$ modern Earth S_{org} flux are compared in Figure 4. For the JWST NIRISS and NIRSpec coverage below $5 \mu\text{m}$, all of our Hycean K2-18 b models with methanogenic flux produce CH_4 absorption features between 1 and $4 \mu\text{m}$ that are broadly consistent with the JWST data. However, it is challenging

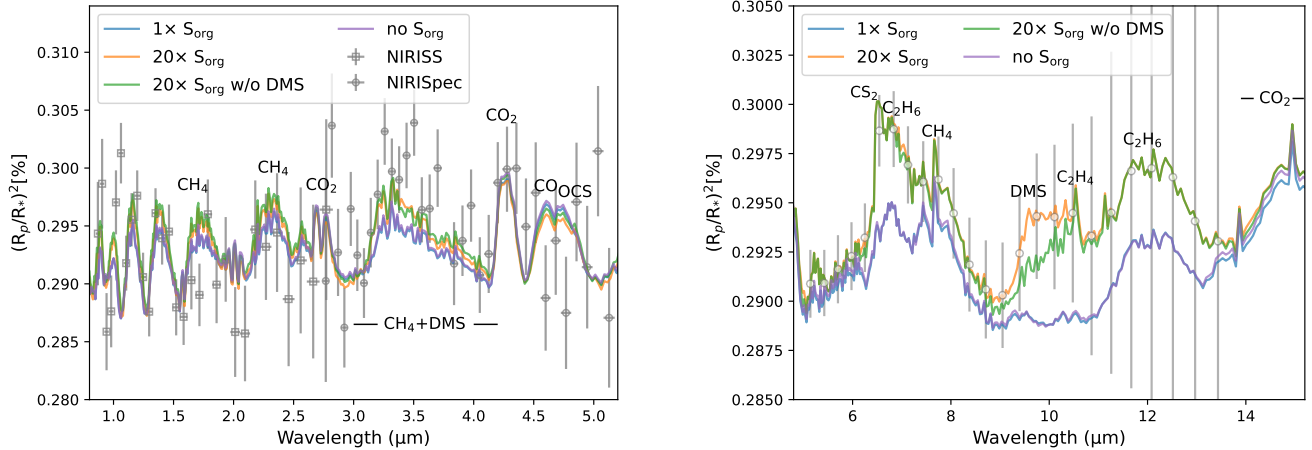


Figure 4. Synthetic transmission spectra of Hycean K2-18 b 1D models for $1\times$ and $20\times$ modern Earth biological sulfur flux. The JWST NIRISS/SOSS and NIRSpec/G395H data from (Madhusudhan et al. 2023) are plotted in the left panel. The simulated noise by Pandexo (Batalha et al. 2017) with the JWST/MIRI LRS for 5 transits without random noise is plotted in the right panel (gray error bars). The $20\times S_{\text{org}}$ spectrum but with DMS opacity removed is shown for comparison. The “no S_{org} ” case includes a flux for CH_4 equivalent to Modern Earth’s non-anthropogenic emission (Domagal-Goldman et al. 2011), but omits fluxes for all biogenic sulfur gases. The corresponding abundance profiles used to produce the spectra can be found in Figure A3.

to distinguish the DMS absorption contribution within the NIRSpec coverage, even with $20\times S_{\text{org}}$ flux. The signal of DMS around $3.5 \mu\text{m}$ for $20\times S_{\text{org}}$ flux does not exceed 10 ppm, smaller than NIRSpec’s precision of 30–50 ppm at $R \sim 50$ (Madhusudhan et al. 2023). The most promising diagnostics window of DMS is in the mid-infrared, as indicated in the right panel of Figure 4. For the $20\times S_{\text{org}}$ case, DMS and the photochemical byproduct C_2H_4 contribute to an absorption of about 50 ppm at 9–11 μm , in addition to the C_2H_6 feature at $7\mu\text{m}$. The $7\text{-}\mu\text{m}$ feature of C_2H_6 also overlaps with CS_2 , making it difficult to differentiate the contribution of CS_2 . Our transmission spectra reveal no discernible H_2S spectral signatures. While H_2S can reach above ppm levels with outgassing and photochemical sources (e.g. pathway (1)), its broad opacities that overlap with several species make it challenging to detect.

Since ethane (C_2H_6) is efficiently produced from CH_4 and has strong mid-infrared absorption bands, C_2H_6 shows a prominent feature at 7 and 11–13 μm with or without the presence of S_{org} flux. By constraining $[\text{CH}_4]/[\text{C}_2\text{H}_6]$, one can potentially estimate the relative contribution of methanogenic CH_4 flux relative to S_{org} flux (Domagal-Goldman et al. 2011). Since our model likely overpredicts C_6H_6 in the gas phase due to the lack of conversion to higher-order hydrocarbons and particles, we did not include C_6H_6 opacities when generating the spectra in Figure 4. However, it is interesting to keep in mind that the presence ($\gtrsim 50$ ppm) of C_6H_6 would exhibit detectable features within NIRSpec wavelength range, in addition to CH_4 and CO_2 (see Figure A4). For biogenic flux $\gtrsim 30\times$ Earth’s S_{org} flux, the atmospheric mean molecular weight exceeds 8 amu in addition to the expected aerosols that would flatten transmission spectral features, making it immediately distinguishable for $\lesssim 20\times$ cases. We summarize the identifiable biosignature features with $1\times$ – $20\times S_{\text{org}}$ flux in Table 1.

4. DISCUSSION

Since K2-18 b requires reflective clouds and hazes to sustain water oceans, we explore the potential UV shielding effects due to clouds and hazes in the bottom panel of Figure 2. Organic sulfur species only start to build up when the stellar UV is reduced to less than 20%. For K2-18 b specifically, Leconte et al. (2024) highlighted the observed methane features deeper than ~ 100 ppm (their Fig. 9) are not consistent with highly reflective clouds. We argue that our photochemical results should remain robust to UV attenuation by clouds and hazes, unless muted spectral features indicate scattering by high-altitude aerosols can significantly reduce stellar UV flux.

The predicted requirement of $20\times S_{\text{org}}$ flux to be potentially detectable is equivalent to about 0.004 g m^{-2} based on the DMS lab production rate (Seager et al. 2013), which is within the plausible range of surface biomass density. Our predictions for the biogenic sulfur gases in Hycean atmospheres are broadly consistent with previous studies of

Table 1. Detectability of potential biosignature gases with corresponding wavelength ranges on Hycean K2-18 b based on our models with $1\times-20\times S_{\text{org}}$ flux. ✓ denotes detectable ($\gtrsim 50$ ppm) and ✗ denotes nondetectable ($\lesssim 10$ ppm), whereas ? means challenging, with shallow features ($\gtrsim 20$ ppm but $\lesssim 50$ ppm) and only present under enhanced $20\times S_{\text{org}}$ flux.

Species	1–5 μm	5–15 μm
CH ₄	✓	✓
CO ₂	✓	✓
H ₂ S	✗	✗
CH ₃ SH	✗	✗
CS ₂	✗	?
DMS	✗	?
DMDS	✗	✗
C ₂ H ₄	✗	?
C ₂ H ₆	✗	✓

the Archean Earth Domagal-Goldman et al. (2011) and Archean-like atmospheres on Trappist-1 planets (Meadows et al. 2023). While Meadows et al. (2023) concluded CH₃SH to be the most prominent S_{org} feature in N₂-dominated atmospheres, we find efficient CH₃SH conversion into H₂S in a H₂ atmosphere. Consequently, DMS appears to constitute the most detectable organic sulfur molecule in the mid-infrared for Hycean worlds.

On modern Earth, the oxidation of DMS might participate in the sulfuric cloud formation (Charlson et al. 1987) and affect climate feedback. It has been suggested that this biologically driven feedbacks could help stabilize the Earth’s climate (Lovelock 1989), although the precise pathways and quantified contributions from DMS to aerosols still remain elusive. Similarly, on a Hycean world with highly elevated S_{org} flux ($\gtrsim 30\times$ modern Earth’s value, see Figure 1.), hydrocarbon and elemental sulfur hazes (S₈) are expected to form. We speculate a similar negative feedback loop can take place in a Hycean world, where photochemical hazes derived from organic sulfur flux can increase albedo and prevent a runaway state.

Lastly, we reiterate that constructing complete line lists for DMS, DMDS, and CH₃SH to correctly account for the pressure-broadening effects would improve the interpretation of spectral data. Future work extending the study encompassing the diversity of halomethanes, such as methyl chloride and methyl bromide (e.g., Leung et al. 2022), will expand our understanding of the biosignature gases on sub-Neptune waterworlds.

5. CONCLUSION

We find a biogenic sulfur flux of approximately 20 times higher than modern Earth’s is required for DMS to reach detectable levels (i.e. above \sim ppm) on a K2-18b-like Hycean world. At the terminators, our 2D photochemical model shows only minor abundance enhancements in DMS compared to 1D model predictions. On the other hand, JWST/MIRI could detect C₂H₆ around 7 μm and the broad feature at 9–13 μm contributed from DMS, C₂H₄, and C₂H₆ with $20\times S_{\text{org}}$ flux, based on our fiducial Hycean model. However, identifying DMS signatures within NIRSpec’s wavelength range is demonstrated to be challenging, despite DMS appearing as the most promising biogenic sulfur signature directly from the S_{org} source. The moderate threshold for biological production suggests that the search for biogenic sulfur gases as one class of potential biosignature is plausible for Hycean worlds.

The authors thank Michaela Leung for the useful comments on an early draft of this article. The authors also thank Stephen Klippenstein and Julie I. Moses for the illuminating discussion on H₂CO kinetics and for sharing the ab initio calculations. S.-M.T. thanks Eva-Maria Ahrer, Guangwei Fu, Jake Taylor, and Lili Alderson for helpful discussions on data resampling and feature identification. S.-M.T. and E.W.S. acknowledge support from National Aeronautics and Space Administration (NASA) through Exobiology Grant No. 80NSSC20K1437 and Interdisciplinary Consortia for Astrobiology Research (ICAR) Grant Nos. 80NSSC23K1399, 80NSSC21K0905, and 80NSSC23K1398. H.I. is funded by the European Union (ERC, DIVERSE, 101087755 and ERC, EXOCONDENSE, 740963). Views and opinions expressed are however those of the author(s) only and do not necessarily reflect those of the European Union or the European Research Council Executive Agency. Neither the European Union nor the granting authority can be held responsible for them. N.F.W. was supported by the NASA Postdoctoral Program.

Software: Exo-FMS ([Lee et al. 2020, 2021](#)), VULCAN ([Tsai et al. 2017, 2021](#)), Numpy ([van der Walt et al. 2011](#))

APPENDIX

A. MODEL INPUT PARAMETERS

Table A1 lists the input parameters for Hycean K2-18 b with the HELIOS radiative transfer model and the ExoFMS general circulation model. HELIOS includes H₂O, CH₄, CO, CO₂, NH₃, HCN, C₂H₂, collision-induced absorption (CIA) of H₂–H₂ and H₂–He as opacity sources. We ignore the H₂O self continuum absorption and likely underestimate the tropospheric temperature. ExoFMS uses double-gray opacities for its radiative transfer. The optical depth in the infrared (τ_{IR}) and shortwave (τ_{SW}) bands is given by:

$$d\tau_i = (\kappa_{i,d}(1 - q) + \kappa_{i,w}q)(f_i + 2(1 - f_i))\left(\frac{p}{p_s}\right)\frac{dp}{g}, \quad (\text{A1})$$

where the i subscript represents either the SW or IR band, p is the pressure and p_s the surface pressure. The opacities $\kappa_{i,w}$ and $\kappa_{i,d}$ represent the opacities due to the water vapour component and dry component (all other gases) of the atmosphere respectively. The factor f_i accounts for pressure dependence of opacity, due to collision-induced absorption and pressure broadening effects. To reproduce the inversion in the HELIOS calculations, a second band was added in the SW part of the spectrum, receiving a fraction α of the total incoming flux. The optical depth in this band was given by:

$$\tau_{\text{SW},2} = \frac{\kappa_{\text{SW},2}p}{g}. \quad (\text{A2})$$

The water mass concentration, q , used in this calculation is taken from the 1D HELIOS calculation and remains constant throughout the simulation (though in reality this should be spatially inhomogeneous and linked to the local saturation vapour pressure at a given temperature and pressure). The value of $\kappa_{\text{IR},w}$ was taken to match the runaway greenhouse OLR of $\approx 280 \text{ Wm}^{-2}$ (as in Innes et al. 2023). The other values were tuned to match the HELIOS temperature-pressure profile. The parameters used are shown in Table A2.

Table A1. Planetary parameters for Hycean K2-18 b.

Symbol	Value	Unit	Description
R_p	1.66×10^7	m	Planetary radius
a	0.1591	AU	Orbital distance
T_{irr}	1370	K	Irradiation temperature
T_{int}	0	K	Internal temperature
g	12.43	m s^{-2}	Gravitational acceleration
c_p	2216	$\text{J K}^{-1} \text{kg}^{-1}$	Specific heat capacity
Ω_p	2.2137×10^{-6}	rad s^{-1}	Planetary rotation rate

Table A2. Radiative parameters for the ExoFMS double-gray radiation scheme.

Symbol	Value	Unit	Description
$\kappa_{\text{IR},d}$	1.15×10^{-3}	$\text{m}^2 \text{kg}^{-1}$	IR dry opacity
$\kappa_{\text{IR},w}$	1×10^{-2}	$\text{m}^2 \text{kg}^{-1}$	IR water opacity
$\kappa_{\text{SW},d}$	2×10^{-5}	$\text{m}^2 \text{kg}^{-1}$	SW dry opacity
$\kappa_{\text{SW},w}$	4×10^{-4}	$\text{m}^2 \text{kg}^{-1}$	SW water opacity
$\kappa_{\text{SW},2}$	5×10^{-2}	$\text{m}^2 \text{kg}^{-1}$	SW second band opacity
α	1×10^{-2}	Dimensionless	Fraction of instellation in SW second band
f_{IR}	0.9	Dimensionless	Controls pressure dependence of τ_{IR}
f_{SW}	0.2	Dimensionless	Controls pressure dependence of τ_{SW}

Table A3. Lower boundary conditions for photochemical modeling of inhabited Hycean K2-18 b.

Species	Surface Emission (molecules cm ⁻² s ⁻¹)	Vdep (cm s ⁻¹)
CH ₄ ^a	7 × 10 ¹⁰	0
CH ₃ SH ^a	8.3 × 10 ⁸	0
DMS ^a	4.2 × 10 ⁹	0 ^d
CS ₂ ^a	1.4 × 10 ⁷	0
H ₂ S ^b	2 × 10 ⁸	0.015
SO ₂ ^b	9 × 10 ⁹	1
COS ^b	5.4 × 10 ⁷	0.003
H ₂ O ₂ ^c	0	1
CH ₃ S ^a	0	0.01
HSO ^a	0	1
S ^a	0	1
SO ^a	0	0.0003

^a Domagal-Goldman et al. (2011)

^b Seinfeld & Pandis (2016)

^c Hauglustaine et al. (1994)

^d For the scenario that the surface layer of the ocean is saturated. The measured deposition velocity of DMS on land is 0.064–0.28 cm s⁻¹ (Judeikis & G. Wren 1977).

B. UPDATED H₂CO REACTION RATES

Formaldehyde (H₂CO) is one of the main intermediate species in CO₂-CO-CH₄ interconversion. Forming and breaking the double bond between C and O in H₂CO may facilitate an important step that controls the overall timescale (Tsai et al. 2018). There are two three-body reactions involving H₂CO that we adopt the thermal dissociation rate coefficients due to the lack of low-pressure rate limits for recombination:



and



The recombination rates are then reversed by thermochemical data. In the default chemical networks in VULCAN (e.g. NCHO_photo_network), the adopted rate coefficients either underestimate the activation energy or are only valid at high temperatures. As a result, these reversed rates tend to overpredict the CO₂-CH₄ conversion efficiency around room temperatures. In this study, we have adopted the low-pressure rate coefficients for B3 and B4 from Tsang & Hampson (1986) and Tsang (1987), which are more consistent with the ab initio calculations conducted by Klippenstein (2023). The original and updated rate coefficients are summarized in Table A4. This update of H₂CO kinetics significantly lowers the CH₄ abundance in our lifeless case (without methanogenic flux; Figure A1) from ~10⁻⁵ to ~10⁻⁸, which is consistent with the calculations in Wogan et al. (2024).

REFERENCES

- Arney, G., Domagal-Goldman, S. D., & Meadows, V. S. 2018, *Astrobiology*, 18, 311, doi: [10.1089/ast.2017.1666](https://doi.org/10.1089/ast.2017.1666)
- Batalha, N. E., Mandell, A., Pontoppidan, K., et al. 2017, *PASP*, 129, 064501, doi: [10.1088/1538-3873/aa65b0](https://doi.org/10.1088/1538-3873/aa65b0)
- Baulch, D. L., Cobos, C. J., Cox, R. A., et al. 1994, *Journal of Physical and Chemical Reference Data*, 23, 847, doi: [10.1063/1.555953](https://doi.org/10.1063/1.555953)
- Bean, J. L., Raymond, S. N., & Owen, J. E. 2021, *Journal of Geophysical Research (Planets)*, 126, e066639, doi: [10.1029/2020JE006639](https://doi.org/10.1029/2020JE006639)
- Benneke, B., Wong, I., Piaulet, C., et al. 2019, *ApJL*, 887, L14, doi: [10.3847/2041-8213/ab59dc](https://doi.org/10.3847/2041-8213/ab59dc)

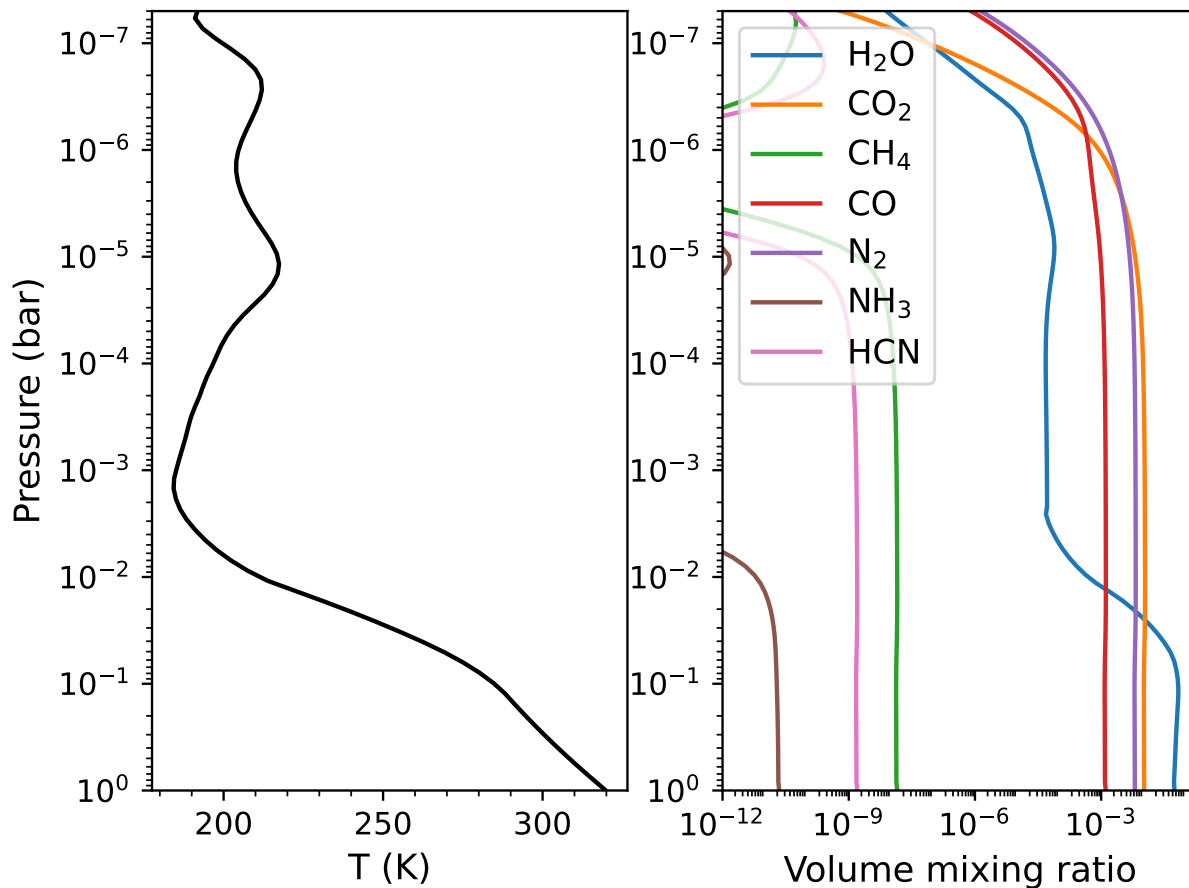


Figure A1. The self-consistent temperature (left) and composition (right) profiles generated by iterative runs between HELIOS and VULCAN. Sulfur kinetics is not included in the VULCAN runs here for simplicity.

Table A4.

Reactions	Rate Coefficients ^a	Reference
Original		
$\text{CH}_2\text{OH} \xrightarrow{\text{M}} \text{H} + \text{H}_2\text{CO}$	$k_0 = 1.66 \times 10^{-10} \exp(-12630/T)$ $k_\infty = 3 \times 10^9 \exp(-14640/T)$	Cribb et al. (1992) Tsuboi et al. (1981)
$\text{CH}_3\text{O} \xrightarrow{\text{M}} \text{H} + \text{H}_2\text{CO}$	$k_0 = 9 \times 10^{-11} \exp(-6790/T)$ $k_\infty = 1.56 \times 10^{15} T^{-0.39} \exp(-13300/T)$	Baulch et al. (1994) Curran (2006)
Updated		
$\text{CH}_2\text{OH} \xrightarrow{\text{M}} \text{H} + \text{H}_2\text{CO}$	$k_0 = 7.48 \times 10^1 T^{-2.5} \exp(-17200/T)$ $k_\infty = 4.53 \times 10^{34} T^{-7.11} \exp(-22200/T)$	Tsang (1987) Xu et al. (2015)
$\text{CH}_3\text{O} \xrightarrow{\text{M}} \text{H} + \text{H}_2\text{CO}$	$k_0 = 6.51 \times 10^{13} T^{-6.65} \exp(-16700/T)$ $k_\infty = 3.17 \times 10^{24} T^{-4.25} \exp(-13100/T)$	Tsang & Hampson (1986) Xu et al. (2015)

^aIn low pressure rate coefficient, k_0 ($\text{cm}^6 \text{ molecules}^{-2} \text{ s}^{-1}$), and high pressure rate coefficient, k_∞ ($\text{cm}^3 \text{ molecules}^{-1} \text{ s}^{-1}$).

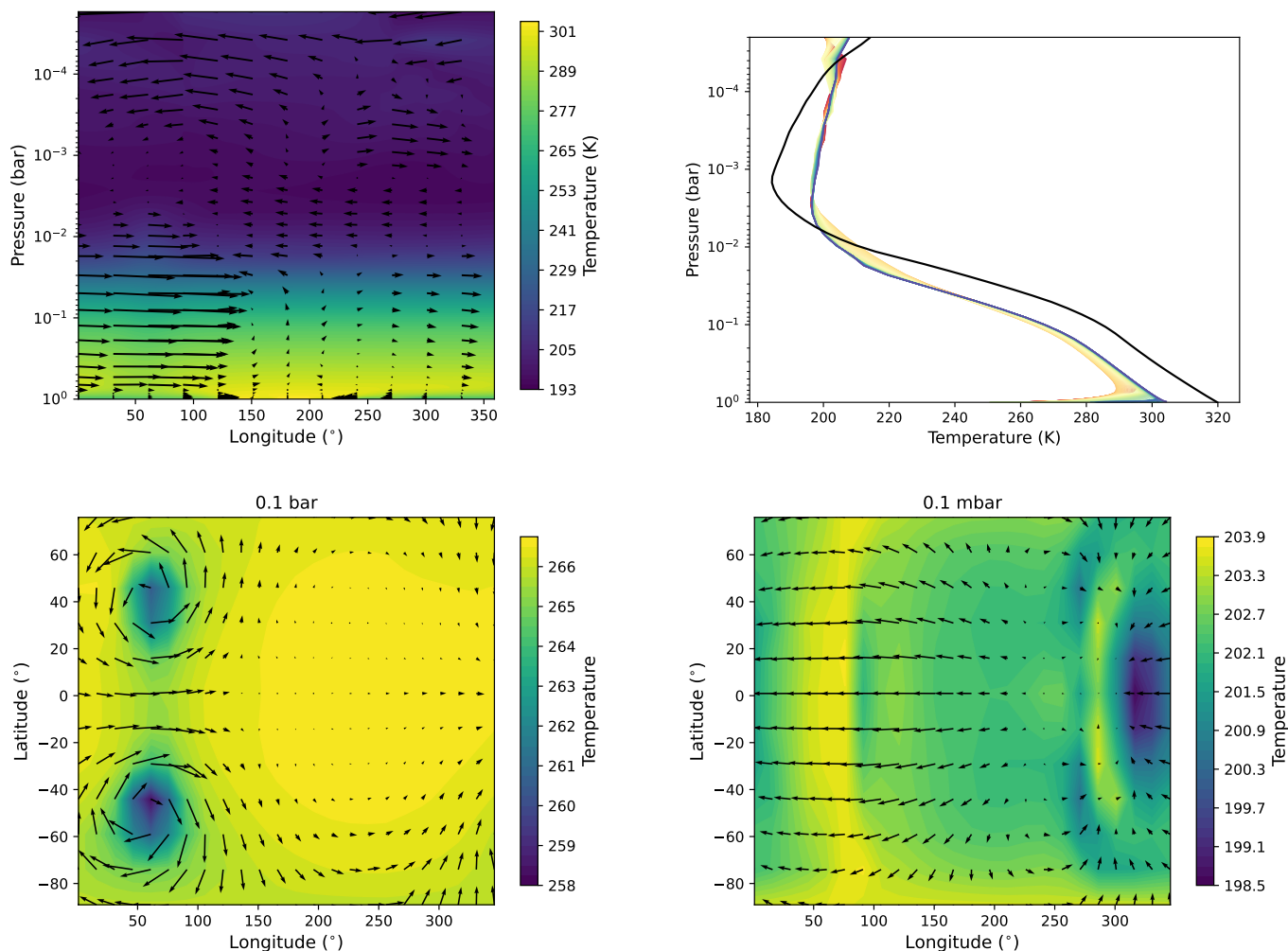


Figure A2. The top left panel shows the temperatures (color scale) and winds (arrows) on the equatorial plane averaged across $\pm 30^\circ$ latitudes from our K2-18 b GCM (substellar point located at 180° longitude). The top right panel displays the vertical temperature profiles around the equator corresponding to different longitudinal locations, where the temperature profile from the 1D radiative transfer calculation (HELIOS) is plotted in black for comparison. The bottom two panels show the temperatures and winds at 0.1 bar and 0.1 mbar level.

Charlson, R. J., Lovelock, J. E., Andreae, M. O., & Warren, S. G. 1987, *Nature*, 326, 655, doi: [10.1038/326655a0](https://doi.org/10.1038/326655a0)

Charnay, B., Meadows, V., & Leconte, J. 2015, *ApJ*, 813, 15, doi: [10.1088/0004-637X/813/1/15](https://doi.org/10.1088/0004-637X/813/1/15)

Chen, H., Wolf, E. T., Kopparapu, R., Domagal-Goldman, S., & Horton, D. E. 2018, *ApJL*, 868, L6, doi: [10.3847/2041-8213/aaedb2](https://doi.org/10.3847/2041-8213/aaedb2)

Cribb, P. H., Dove, J. E., & Yamazaki, S. 1992, *Combustion and Flame*, 88, 169, doi: [https://doi.org/10.1016/0010-2180\(92\)90050-Y](https://doi.org/10.1016/0010-2180(92)90050-Y)

Curran, H. J. 2006, *International Journal of Chemical Kinetics*, 38, 250, doi: <https://doi.org/10.1002/kin.20153>

Domagal-Goldman, S. D., Meadows, V. S., Claire, M. W., & Kasting, J. F. 2011, *Astrobiology*, 11, 419, doi: [10.1089/ast.2010.0509](https://doi.org/10.1089/ast.2010.0509)

Esparza-Borges, E., López-Morales, M., Adams Redai, J. I., et al. 2023, *ApJL*, 955, L19, doi: [10.3847/2041-8213/acf27b](https://doi.org/10.3847/2041-8213/acf27b)

France, K., Loyd, R. O. P., Youngblood, A., et al. 2016, *ApJ*, 820, 89, doi: [10.3847/0004-637X/820/2/89](https://doi.org/10.3847/0004-637X/820/2/89)

Gueymard, C. A. 2018, *Solar Energy*, 169, 434, doi: <https://doi.org/10.1016/j.solener.2018.04.067>

Hammond, M., Tsai, S.-M., & Pierrehumbert, R. T. 2020, *ApJ*, 901, 78, doi: [10.3847/1538-4357/abb08b](https://doi.org/10.3847/1538-4357/abb08b)

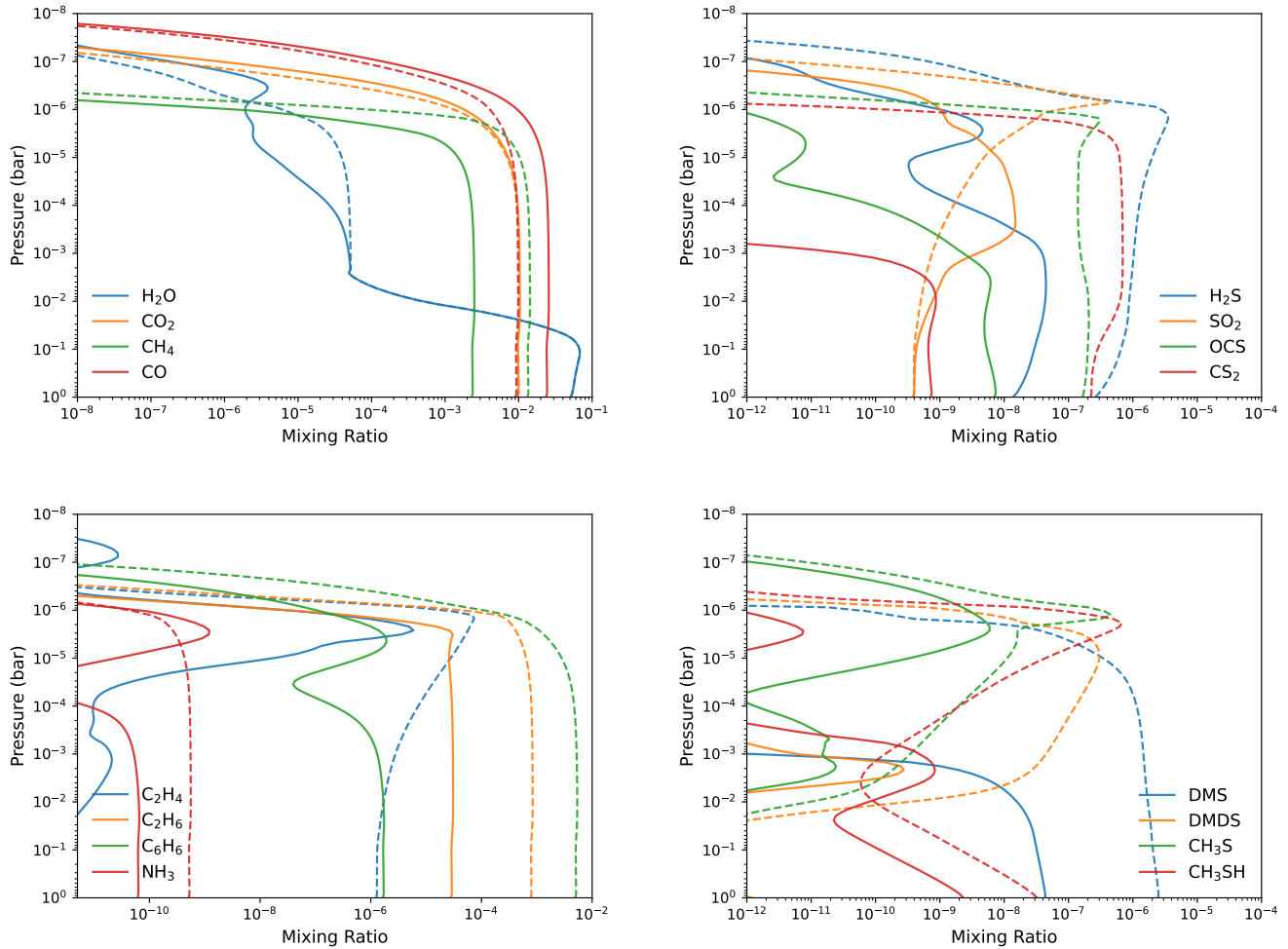


Figure A3. The abundance profiles of the Hycean K2-18 b 1D models with $1\times$ (solid) and $20\times$ (dashed) modern Earth values.

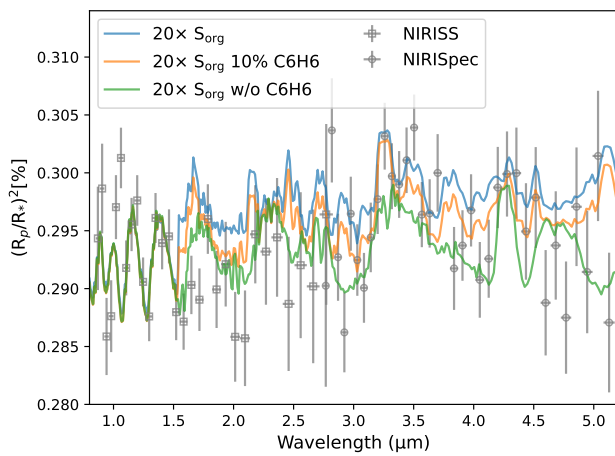


Figure A4. Synthetic transmission spectra of Hycean K2-18 b similar to Figure 4, but including C_6H_6 absorption for $20\times S_{org}$ flux. The spectra without C_6H_6 opacity and with 10% of C_6H_6 , representing depletion from haze formation, are shown for comparison.

Hauglustaine, D. A., Granier, C., Brasseur, G. P., & Mège, G. 1994, *J. Geophys. Res.*, 99, 1173, doi: [10.1029/93JD02987](https://doi.org/10.1029/93JD02987)

House, C. H., Runnegar, B., & Fitz-Gibbon, S. T. 2003, *Geobiology*, 1, 15, doi: [10.1046/j.1472-4669.2003.00004.x](https://doi.org/10.1046/j.1472-4669.2003.00004.x)

- Howard, A. W., Marcy, G. W., Bryson, S. T., et al. 2012, *ApJS*, 201, 15, doi: [10.1088/0067-0049/201/2/15](https://doi.org/10.1088/0067-0049/201/2/15)
- Hu, R., Damiano, M., Scheucher, M., et al. 2021, 921, L8, doi: [10.3847/2041-8213/ac1f92](https://doi.org/10.3847/2041-8213/ac1f92)
- Hu, R., Seager, S., & Bains, W. 2012, *Astrophys. J.*, 761, doi: [10.1088/0004-637X/761/2/166](https://doi.org/10.1088/0004-637X/761/2/166)
- Innes, H., & Pierrehumbert, R. T. 2022, *ApJ*, 927, 38, doi: [10.3847/1538-4357/ac4887](https://doi.org/10.3847/1538-4357/ac4887)
- Innes, H., Tsai, S.-M., & Pierrehumbert, R. T. 2023, *ApJ*, 953, 168, doi: [10.3847/1538-4357/ace346](https://doi.org/10.3847/1538-4357/ace346)
- Johnson, T. J., Sams, R. L., & Sharpe, S. W. 2004, in *Society of Photo-Optical Instrumentation Engineers (SPIE) Conference Series*, Vol. 5269, Chemical and Biological Point Sensors for Homeland Defense, ed. I. Sedlacek, Arthur J., R. Colton, & T. Vo-Dinh, 159–167, doi: [10.1117/12.515604](https://doi.org/10.1117/12.515604)
- Judekikis, H. S., & G. Wren, A. 1977, *Atmospheric Environment* (1967), 11, 1221, doi: [https://doi.org/10.1016/0004-6981\(77\)90099-3](https://doi.org/10.1016/0004-6981(77)90099-3)
- Kettle, A. J., Rhee, T. S., von Hobe, M., et al. 2001, *J. Geophys. Res.*, 106, 12,193, doi: [10.1029/2000JD900630](https://doi.org/10.1029/2000JD900630)
- Kite, E. S., & Ford, E. B. 2018, *ApJ*, 864, 75, doi: [10.3847/1538-4357/aad6e0](https://doi.org/10.3847/1538-4357/aad6e0)
- Klippenstein, S. J. 2023, Private Communication
- Leconte, J., Spiga, A., Clément, N., et al. 2024, arXiv e-prints, arXiv:2401.06608, doi: [10.48550/arXiv.2401.06608](https://doi.org/10.48550/arXiv.2401.06608)
- Lee, E. K. H., Parmentier, V., Hammond, M., et al. 2021, *MNRAS*, 506, 2695. <https://arxiv.org/abs/2106.11664>
- Lee, G. K., Casewell, S. L., Chubb, K. L., et al. 2020, *Monthly Notices of the Royal Astronomical Society*, 496, 4674, doi: [10.1093/mnras/staa1882](https://doi.org/10.1093/mnras/staa1882)
- Leung, M., Schwieterman, E. W., Parenteau, M. N., & Faucher, T. J. 2022, *ApJ*, 938, 6, doi: [10.3847/1538-4357/ac8799](https://doi.org/10.3847/1538-4357/ac8799)
- Li, C.-Y., Cao, H.-Y., Wang, Q., et al. 2023, *The ISME Journal*, 17, 1184, doi: [10.1038/s41396-023-01430-z](https://doi.org/10.1038/s41396-023-01430-z)
- Lovelock, J. E. 1989, *Reviews of Geophysics*, 27, 215, doi: [10.1029/RG027i002p00215](https://doi.org/10.1029/RG027i002p00215)
- Loyd, R. O. P., France, K., Youngblood, A., et al. 2016, *ApJ*, 824, 102, doi: [10.3847/0004-637X/824/2/102](https://doi.org/10.3847/0004-637X/824/2/102)
- Luque, R., & Pallé, E. 2022, *Science*, 377, 1211, doi: [10.1126/science.abl7164](https://doi.org/10.1126/science.abl7164)
- Madhusudhan, N., Nixon, M. C., Welbanks, L., Piette, A. A., & Booth, R. A. 2020, *ApJL*, 891, L7, doi: [10.3847/2041-8213/ab7229](https://doi.org/10.3847/2041-8213/ab7229)
- Madhusudhan, N., Piette, A. A. A., & Constantinou, S. 2021, *ApJ*, 918, 1, doi: [10.3847/1538-4357/abfd9c](https://doi.org/10.3847/1538-4357/abfd9c)
- Madhusudhan, N., Sarkar, S., Constantinou, S., et al. 2023, *ApJL*, 956, L13, doi: [10.3847/2041-8213/acf577](https://doi.org/10.3847/2041-8213/acf577)
- Malik, M., Kempton, E. M. R., Koll, D. D. B., et al. 2019b, *ApJ*, 886, 142, doi: [10.3847/1538-4357/ab4a05](https://doi.org/10.3847/1538-4357/ab4a05)
- Malik, M., Kitzmann, D., Mendonça, J. M., et al. 2019a, *The Astronomical Journal*, 157, 170, doi: [10.3847/1538-3881/ab1084](https://doi.org/10.3847/1538-3881/ab1084)
- Mateos, K., Chappell, G., Klos, A., et al. 2023, *Science Advances*, 9, eade4847, doi: [10.1126/sciadv.ade4847](https://doi.org/10.1126/sciadv.ade4847)
- Meadows, V., Lincowski, A., & Lustig-Yaeger, J. 2023, in *American Astronomical Society Meeting Abstracts*, Vol. 55, American Astronomical Society Meeting Abstracts, 125.04
- Nixon, M. C., & Madhusudhan, N. 2021, *MNRAS*, 505, 3414, doi: [10.1093/mnras/stab1500](https://doi.org/10.1093/mnras/stab1500)
- Peacock, S., Barman, T., Shkolnik, E. L., et al. 2020, *ApJ*, 895, 5, doi: [10.3847/1538-4357/ab893a](https://doi.org/10.3847/1538-4357/ab893a)
- Pierrehumbert, R. T. 2023, *ApJ*, 944, 20, doi: [10.3847/1538-4357/acafdf](https://doi.org/10.3847/1538-4357/acafdf)
- Piette, A. A. A., & Madhusudhan, N. 2020, *ApJ*, 904, 154, doi: [10.3847/1538-4357/abfbf1](https://doi.org/10.3847/1538-4357/abfbf1)
- Pilcher, C. B. 2003, *Astrobiology*, 3, 471, doi: [10.1089/153110703322610582](https://doi.org/10.1089/153110703322610582)
- Rogers, J. G., Schlichting, H. E., & Owen, J. E. 2023, *ApJL*, 947, L19, doi: [10.3847/2041-8213/acc86f](https://doi.org/10.3847/2041-8213/acc86f)
- Schwieterman, E. W., Kiang, N. Y., Parenteau, M. N., et al. 2018, *Astrobiology*, 18, 663, doi: [10.1089/ast.2017.1729](https://doi.org/10.1089/ast.2017.1729)
- Seager, S., Bains, W., & Hu, R. 2013, *ApJ*, 777, 95, doi: [10.1088/0004-637X/777/2/95](https://doi.org/10.1088/0004-637X/777/2/95)
- Seinfeld, J. H., & Pandis, S. N. 2016, *Atmospheric chemistry and physics: from air pollution to climate change* (John Wiley & Sons, Inc.)
- Smith, M. D. 1998, *Icarus*, 132, 176, doi: <https://doi.org/10.1006/icar.1997.5886>
- Thompson, S. E., Coughlin, J. L., Hoffman, K., et al. 2018, *ApJS*, 235, 38, doi: [10.3847/1538-4365/aab4f9](https://doi.org/10.3847/1538-4365/aab4f9)
- Tsai, S.-M., Dobbs-Dixon, I., & Gu, P.-G. 2014, *ApJ*, 793, 141, doi: [10.1088/0004-637X/793/2/141](https://doi.org/10.1088/0004-637X/793/2/141)
- Tsai, S.-M., Innes, H., Lichtenberg, T., et al. 2021b, *The Astrophysical Journal Letters*, 922, L27, doi: [10.3847/2041-8213/ac399a](https://doi.org/10.3847/2041-8213/ac399a)
- Tsai, S.-M., Kitzmann, D., Lyons, J. R., et al. 2018, *ApJ*, 862, 31, doi: [10.3847/1538-4357/aac834](https://doi.org/10.3847/1538-4357/aac834)
- Tsai, S.-M., Lyons, J. R., Grosheintz, L., et al. 2017, *Astrophys. J. Suppl. Ser.*, 228, 1, doi: [10.3847/1538-4365/228/2/20](https://doi.org/10.3847/1538-4365/228/2/20)
- Tsai, S.-M., Malik, M., Kitzmann, D., et al. 2021, *The Astrophysical Journal*, 923, 264, doi: [10.3847/1538-4357/ac29bc](https://doi.org/10.3847/1538-4357/ac29bc)

- Tsai, S.-M., Moses, J. I., Powell, D., & Lee, E. K. H. 2023c, *ApJL*, 959, L30, doi: [10.3847/2041-8213/ad1405](https://doi.org/10.3847/2041-8213/ad1405)
- Tsai, S.-M., Parmentier, V., Mendonça, J. M., et al. 2024, arXiv e-prints, arXiv:2310.17751, doi: [10.48550/arXiv.2310.17751](https://doi.org/10.48550/arXiv.2310.17751)
- Tsang, W. 1987, *Journal of Physical and Chemical Reference Data*, 16, 471, doi: [10.1063/1.555802](https://doi.org/10.1063/1.555802)
- Tsang, W., & Hampson, R. F. 1986, *Journal of Physical and Chemical Reference Data*, 15, 1087, doi: [10.1063/1.555759](https://doi.org/10.1063/1.555759)
- Tsiaras, A., Waldmann, I. P., Tinetti, G., Tennyson, J., & Yurchenko, S. N. 2019, *Nature Astronomy*, 3, 1086, doi: [10.1038/s41550-019-0878-9](https://doi.org/10.1038/s41550-019-0878-9)
- Tsuboi, T., Katoh, M., Kikuchi, S., & Hashimoto, K. 1981, *Japanese Journal of Applied Physics*, 20, 985, doi: [10.1143/JJAP.20.985](https://doi.org/10.1143/JJAP.20.985)
- van der Walt, S., Colbert, S. C., & Varoquaux, G. 2011, *Computing in Science Engineering*, 13, 22, doi: [10.1109/MCSE.2011.37](https://doi.org/10.1109/MCSE.2011.37)
- Venturini, J., Guilera, O. M., Haldemann, J., Ronco, M. P., & Mordasini, C. 2020, *A&A*, 643, L1, doi: [10.1051/0004-6361/202039141](https://doi.org/10.1051/0004-6361/202039141)
- Wogan, N. F., Batalha, N. E., Zahnle, K. J., et al. 2024, *ApJL*, 963, L7, doi: [10.3847/2041-8213/ad2616](https://doi.org/10.3847/2041-8213/ad2616)
- Xu, Z. F., Raghunath, P., & Lin, M. C. 2015, *Journal of Physical Chemistry A*, 119, 7404, doi: [10.1021/acs.jpca.5b00553](https://doi.org/10.1021/acs.jpca.5b00553)
- Youngblood, A., France, K., Loyd, R. O. P., et al. 2016, *ApJ*, 824, 101, doi: [10.3847/0004-637X/824/2/101](https://doi.org/10.3847/0004-637X/824/2/101)
- Yu, X., Moses, J. I., Fortney, J. J., & Zhang, X. 2021, *ApJ*, 914, 38, doi: [10.3847/1538-4357/abfdc7](https://doi.org/10.3847/1538-4357/abfdc7)
- Zeng, L., Jacobsen, S. B., Sasselov, D. D., et al. 2019, *Proceedings of the National Academy of Science*, 116, 9723, doi: [10.1073/pnas.1812905116](https://doi.org/10.1073/pnas.1812905116)
- Zhang, M., Chachan, Y., Kempton, E. M. R., & Knutson, H. A. 2019, *PASP*, 131, 034501, doi: [10.1088/1538-3873/aaf5ad](https://doi.org/10.1088/1538-3873/aaf5ad)
- Zhang, M., Chachan, Y., Kempton, E. M. R., Knutson, H. A., & Chang, W. H. 2020, *ApJ*, 899, 27, doi: [10.3847/1538-4357/ab1e6](https://doi.org/10.3847/1538-4357/ab1e6)
- Zhang, M., Park, K.-T., Yan, J., et al. 2020, *Progress in Oceanography*, 186, 102392, doi: <https://doi.org/10.1016/j.pocean.2020.102392>